Applied Surface Science 463 (2019) 1001–1010

Contents lists available at ScienceDirect

Applied Surface Science

journal homepage: www.elsevier.com/locate/apsusc

Full Length Article

Improving electrochemical activity of activated carbon derived from popcorn by $NiCo_2S_4$ nanoparticle coating

Miao Yu, Yingying Han, Yao Li, Jian Li, Lijuan Wang*

Key Laboratory of Bio-based Materials Science and Technology of Ministry of Education, Northeast Forestry University, Harbin, PR China
Research Center of Wood Intelligent Science, Northeast Forestry University, Harbin, PR China

ARTICLE INFO

Keywords:
Popcorn
Activated carbon
$NiCo_2S_4$
Supercapacitors

ABSTRACT

We report a popcorn-derived activated carbon (PCs) from maize grains. Dispersed $NiCo_2S_4$ nanoparticles of dozens of nanometers in diameter are anchored onto the PC surface to yield PCs/$NiCo_2S_4$ composites. The adhesion of $NiCo_2S_4$ nanoparticles to the porous carbon substrate provides the PCs/$NiCo_2S_4$ composite electrode with an improved electrochemical performance. The highly electroconductive PCs substrate with porous structure and combination with dispersive $NiCo_2S_4$ nanoparticles, yields PCs/$NiCo_2S_4$ composites with a high specific capacitance of 605.2 F g^{-1} at the current density of 0.5 A g^{-1} in a voltage range of −0.1 to 0.4 V in 6 M KOH electrolyte, and an outstanding capacitance conservation of 91.3% after 5000 galvanostatic charge/discharge cycling. Moreover, the asymmetric supercapacitor demonstrates high energy density of 23.3 W h kg^{-1} at the power density of 335.8 W kg^{-1}, and an excellent cycling stability of 92.7% capacitance retention after 5000 cycles. This research supplies a novel method to exploit biomass-based electrode material candidates for promising application on high-performance supercapacitors.

1. Introduction

In the last few years, global warming and the growing amount of fossil-fuel depletion has raised great interest and effort towards the development of alternative sustainable and renewable energy sources [1,2]. Of the several kinds of important energy-storage devices, supercapacitors which are also termed electrochemical capacitors, have gained increasing attention because of their advantages, such as high power densities, a long cycling life, a rapid charge-discharge rate, and safe pollution-free operation over batteries and conventional physical capacitors [3–5]. These supercapacitors show greatly potentially application in the power source supplementation, electric vehicles and digital devices [6–8], Based on the different charge storage mechanism, supercapacitors may be classified into two categories electrical double-layer capacitors (EDLCs) and pseudocapacitors [9]. In EDLCs, energy storage derives from the electron diffusion and accumulation of charges at the electrode/electrolyte interface. Many carbon-based materials, such as activated carbon [10], graphene [11–13], carbon nanotubes [14], carbon fibers [15,16], carbon aerogels [17,18], and mesoporous carbon [19–21] have been employed widely as electrode materials in supercapacitors. Activated carbon with a high surface area can offer sufficient adsorbing sites for the interfacial charge accumulation because of their developed porous structure, and thus exhibits a large specific capacitance. However, the stored energy is usually restricted by limited electrical charge separation at the interface. In contrast with EDLCs, pseudocapacitors usually exhibit much higher capacitances, because of the specific energy-storage mechanism by reversible faradaic redox reactions at or near the electrode surface [1]. However, the transition-metal oxides often experience the drawback of a poor electrical conductivity, which impedes the electron transfer, and results in a loss of capacitance [22]. Thus, new electrode materials with a higher capacitance, an enhanced chemical stability and an improved electrical conductivity are urgent needed to develop in order to meet the demands of high-performance supercapacitors. In recent years, transition-metal sulfides like NiS [22], CoS [23], Co_9S_8 [24,25], and $NiCo_2S_4$ [26–28], have gained great attention because of their merits, such as a higher electrical conductivity, a better electrochemical activity, excellent electrochemical properties and their thermal stability. In particular, $NiCo_2S_4$ has been considered the most promising electrode candidate for supercapacitors, and has become a research hotspot in the pseudocapacitor field. For instance, Chen et al. synthesized urchin-like $NiCo_2S_4$ with a high specific capacitance of 1149 F g^{-1} at 1 A g^{-1} and a capacitance retention of 91.4% after 5000 cycles at 20 A g^{-1} [9]. Pu et al. prepared hollow hexagonal $NiCo_2S_4$ nanoplates, showing a

* Corresponding author at: Key Laboratory of Bio-based Materials Science and Technology of Ministry of Education, Northeast Forestry University, Harbin, PR China.
E-mail address: donglinwlj@sohu.com (L. Wang).

https://doi.org/10.1016/j.apsusc.2018.09.037
Received 18 June 2018; Received in revised form 5 September 2018; Accepted 5 September 2018
Available online 06 September 2018
0169-4332/

specific capacitance of 437 F g^{-1} at 1 A g^{-1} [29]. Wan et al. synthesized porous $NiCo_2S_4$ nanotubes via sacrificial templates with a high specific capacitance of 933 F g^{-1} at 1 A g^{-1} [30]. The reason for this behavior may be attributed to the following aspects: firstly, $NiCo_2S_4$ has been proven to exhibit much lower optical bandgap energies with ~100 times of the electrical conductivity than that of the corresponding ternary metal oxide $NiCo_2O_4$ [31]; secondly, in the presence of nickel and cobalt ions, ternary transition-metal sulfide $NiCo_2S_4$ could provide more Faradaic redox reactions than binary transition-metal sulfides, which gives rise to better electrochemical properties.

The puffing effect has been used extensively to prepare three-dimensional edible and degradable foams from starch-based materials. Maize grain has been used widely for popcorn production because of its characteristics, such as its low cost, sustainability, renewability, and environmental friendliness. In general, the grains are ground and heated in a sealed container. Subsequently, the starch-containing feedstocks are extruded at a high temperature and pressure, and they puff instantaneously in a larger space at a decreased pressure to transform into popcorn with a three-dimensional porous structure that can be maintained through a facile carbonization process. Hou et al. prepared porous carbon flakes by using popcorn derived from maize biomass via a bombing process, which showed an ultrahigh specific surface area of 3301 $m^2 g^{-1}$ and an excellent specific capacitance of 286 F g^{-1} for supercapacitors [32]. Liang et al. reported that a steam-explosion popcorn-derived porous carbon that delivered a high specific capacitance of 245 F g^{-1} at 0.5 A g^{-1} and a capacitance conservation of 97.8% after 5000 charge/discharge cycles at the current density of 5 A g^{-1} also showed a CO_2 adsorption capacity of 4.60 mmol g^{-1} at 1066 mbar [33].

In this work, popcorn derived from maize grains has been used as a precursor to prepare activated carbon through the combination of carbonization and alkali-activation processes. Dispersed $NiCo_2S_4$ nanoparticles were applied to the surface of conductive popcorn-derived activated carbon (PCs) by a hydrothermal treatment to form a PCs/$NiCo_2S_4$ composite electrode material which possesses highly porous structures and enhanced reactivity for rapid electrolyte-ion diffusion and charge transfer. The PCs/$NiCo_2S_4$ composite shows a high specific capacitance of 605.2 F g^{-1} at the current density of 0.5 A g^{-1} in the voltage range of −0.1 to 0.4 V in 6 M KOH electrolyte. It also presents a long-term cycling stability with a 91.3% capacity retention after 5000 consecutive charge/discharge cycles. The results demonstrate that the PCs/$NiCo_2S_4$ composite is a potential electrode material in high-performance supercapacitors for energy-storage applications.

2. Materials and methods

2.1. Materials and chemicals

Nickel sulfate hydrate ($NiSO_4{\cdot}6H_2O$) was supplied by Tianda Chemical LLC (Tianjin, China). Urea (CON_2H_4) was bought from Tianli Chemical LLC (Tianjin, China). Potassium hydroxide (KOH) was acquired from Kermel Co., Ltd (Tianjin, China). Cobalt sulfate hydrate ($CoSO_4{\cdot}7H_2O$) was provided by Jinfeng Chemical LLC (Tianjin, China). Sodium sulphide hydrate ($Na_2S{\cdot}9H_2O$) was purchased from Zhiyuan Chemical LLC (Tianjin, China).

2.2. PC preparation

The popcorn was cut into pieces and pre-carbonized at 400 °C for 40 min at a heating rate of 5 °C min^{-1} with N_2 protection. The obtained black bulk was mixed with a KOH solution (3 g g^{-1} black bulk), dried at 80 °C, then transferred to a tube furnace for activation at 800 °C for 1 h with a heating rate of 5 °C min^{-1} under a N_2 atmosphere. Afterwards, the obtained activated carbon was washed with 1 M HCl to eliminate the inorganic impurities, rinsed with deionized water until the filtrate became neutral, and dried at 100 °C overnight. The resulting sample was denoted PCs.

2.3. Preparation of PCs/$NiCo_2S_4$ composite

$NiCo_2S_4$ growth on the PCs was achieved by a hydrothermal process. Typically, 2 mmol of cobalt-sulfate hydrate ($CoSO_4{\cdot}7H_2O$), 1 mmol of nickel-sulfate hydrate ($NiSO_4{\cdot}6H_2O$), and 6 mmol of urea were dispersed in 35 mL of deionized water and stirred for 30 min to acquire a homogeneous solution. This solution was poured into a 50-mL Teflon-lined stainless-steel autoclave and heated at 120 °C for 6 h in an oven and then cooled to room temperature. The obtained product was rinsed repeatedly with deionized water and ethanol, filtered, and dried at 60 °C in an oven overnight. The Ni/Co precursors were obtained.

In the second step, the as-prepared Ni/Co precursors and PCs were immersed in 0.2 M of sodium-sulfide-hydrate ($Na_2S{\cdot}9H_2O$) solution to allow sufficient penetration, transferred into a 50-mL Teflon-lined stainless-steel autoclave, and heated at 120 °C for 12 h. After the solution had cooled to room temperature naturally, the product was rinsed with deionized water and ethanol for three times and dried at 60 °C overnight. The obtained composites were denoted PCs/$NiCo_2S_4$. The mass loading of $NiCo_2S_4$ was measured by the mass difference before and after the hydrothermal process.

2.4. Characterization

The morphologies and structures were observed by a scanning electron microscope (SEM, FEI, Sirion, Netherlands). High-resolution transmission electron microscopy (HR-TEM) images were obtained from a transmission electron microscope (TEM, JEM-2100, Japan). The XRD patterns were measured on a X-ray diffractometer (XRD, Rigaku, D/max 2200, Japan) using Cu Kα radiation under a scanning rate of 5° min^{-1} from 5° to 90°. The surface chemical composition of the PC/$NiCo_2S_4$ composite was measured by X-ray photoelectron spectroscopy (XPS, AXIS Ultra DLD spectrometer) using a monochromatic Al Kα X-ray source. Raman spectra were collected on a laser micro-Raman spectrometry (Thermo Fischer DXR, USA) with an excitation wavelength of 532 nm. N_2 adsorption and desorption tests were carried out on an N_2 adsorption analyzer (ASAP 2020, USA) at −196 °C. The specific surface area of the samples was determined by the Brunauer-Emmet-Teller (BET) method, and pore size distribution was analyzed by the Barrett-Joyner-Halenda (BJH) method.

2.5. Electrochemical measurements

The working electrode was fabricated by mixing the as-prepared active materials with polytetrafluoroethylene (PTEE) and carbon black in a mass ratio of 8:1:1. After intensive mixing, the mixture slurry was pressed onto a piece of Ni foam substrate (0.8 cm × 0.8 cm) as a current collector that had been washed ultrasonically with ethanol, HCl (1 mol L^{-1}) and deionized water. The working electrode was dried at 100 °C for 12 h and compressed at ~1 MPa. Mass loading of the active materials was controlled at ~2 mg and the working area of each electrode was fixed at 0.8 × 0.8 cm^2. All electrochemical tests were carried out on an electrochemical workstation (Corrtest, CS350, China) using 6 M KOH electrolyte in a three-electrode system, where an Ag/AgCl electrode served as a reference electrode and a Pt wire was a counter electrode. The electrochemical performance of the electrode samples was evaluated by cyclic voltammetry (CV), galvanostatic charge/discharge curve (GCD), and electrochemical impedance spectroscopy (EIS). The specific capacitance can be measured from the discharge curves according to the equation [34]: $Cs = (I \times \Delta t)/(m \times \Delta V)$, where Cs is the specific capacitance of the electrode (F g^{-1}), I is the applied current (A), Δt is the discharge time (s), m is the active mass of the sample (g), and ΔV is the operating potential (V). The EIS tests were performed from 10 mHz to 100 kHz with an amplitude of 5 mV.

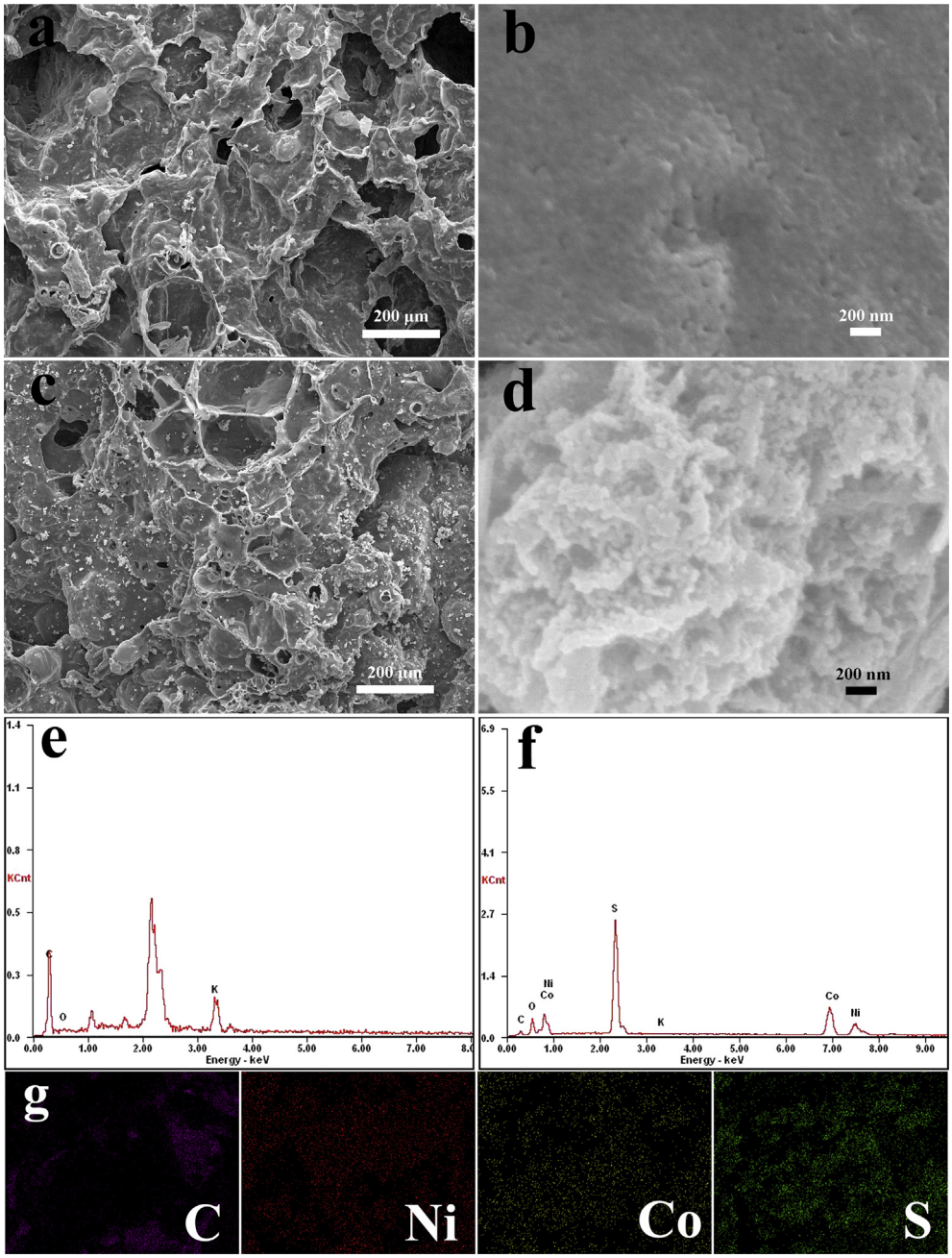

Fig. 1. SEM photographs of (a, b) PCs and (c, d) PCs/$NiCo_2S_4$ composites, EDS spectra of PCs (e) and PC/$NiCo_2S_4$ composites (f), the corresponding EDS elemental mapping of C, Ni, Co and S for PCs/$NiCo_2S_4$ composites (g).

2.6. Electrochemical measurements of the asymmetric supercapacitors

The asymmetric supercapacitor was assembled by using PCs/$NiCo_2S_4$ composites as the positive electrode and PCs as the negative electrode. Energy density and power density of the asymmetric supercapacitor were calculated according to the following equations: $P = E/\Delta t$, $E = (Cs \times \Delta V^2)/2$, where Cs is the specific capacitance of the electrode ($F\,g^{-1}$), ΔV is the operating potential (V), Δt is the discharge time (s), E corresponds to the energy density ($Wh\,kg^{-1}$) and P is the power density ($W\,kg^{-1}$), respectively.

3. Results and discussion

3.1. PCs and PCs/$NiCo_2S_4$ composite morphology

The surface morphology of the PCs and PCs/$NiCo_2S_4$ composites was studied from SEM images (Fig. 1). The pristine PCs show an uneven surface with numerous pores on the walls from the puffing effect. At a higher resolution, the surface presents a highly developed porous structure that was activated by KOH, and which provided the developed surface area and large pore volume. The morphology (Fig. 1c) of the PCs/$NiCo_2S_4$ composite is consistent with that of the PCs at a low magnification, but at a higher magnification (Fig. 1d), ball-like nanoparticles were visible on the carbon surface, which indicates $NiCo_2S_4$ has grown during the hydrothermal process. Energy-dispersive spectroscopy (EDS) confirmed the existence of elemental Ni, Co, S, and C in

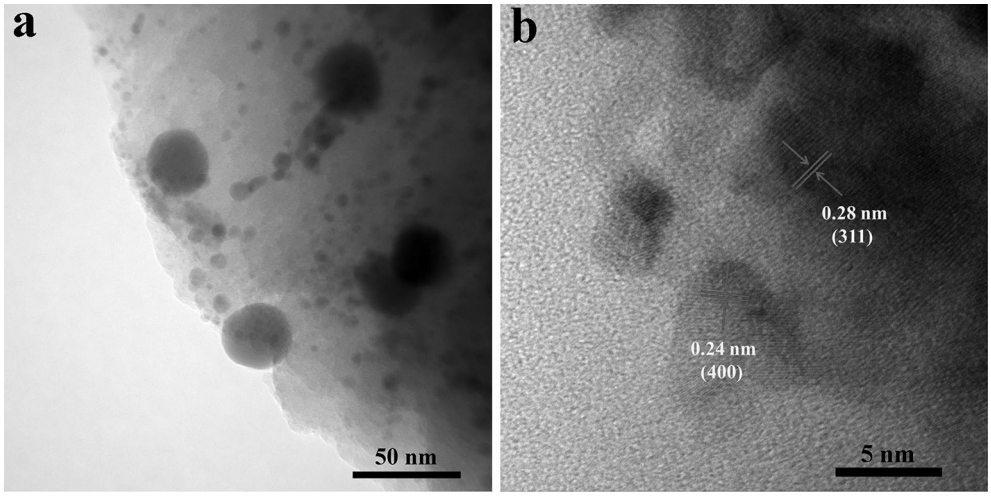

Fig. 2. TEM (a) and HRTEM (b) images of PCs/$NiCo_2S_4$ composites.

the PCs/$NiCo_2S_4$ composites. The corresponding EDS elemental mapping images (Fig. 1g) for PCs/$NiCo_2S_4$ composite confirm the uniform distribution of C, Ni, Co, and S elements. The low and high-magnification TEM photographs of the PCs/$NiCo_2S_4$ composites are presented in Fig. 2 (a) and (b). The TEM photographs confirmed the spherical morphology of the $NiCo_2S_4$ nanoparticles that was visible in the SEM photographs in Fig. 1 (c) and (d). In the PCs/$NiCo_2S_4$ composites, the carbon layer is in intimate contact with the $NiCo_2S_4$ nanoparticles. This unique structure provides a synergistic effect that could provide sufficient active sites and enhance the electrochemical properties of the active material.

3.2. XPS analysis

XPS measurements were performed to determine the superficial element as well as valence states of the PCs/$NiCo_2S_4$ composites. The XPS spectra (Fig. 3) show peaks at 169.6 eV, 781.4 eV, and 855.6 eV, which are corresponded to S 2p, Co 2p, and Ni 2p, respectively, demonstrating the existence of elemental Co, Ni, and S in the PC/$NiCo_2S_4$ composites [35]. The Co 2p and Ni 2p spectra could be well-fitted with two spin orbital doublets and two pairs of shake-up satellites (denoted "Sat.") by using the Gaussian fitting method. As shown in Fig. 3(b), peaks 856.4 eV and 874.3 eV correspond to Ni $2p_{3/2}$ and Ni $2p_{1/2}$, respectively. The distinction of binding energy between Ni $2p_{1/2}$ and Ni $2p_{3/2}$ is 17.9 eV, which indicates the existence of Ni^{2+} and Ni^{3+} in the PCs/$NiCo_2S_4$ composites. For the Co 2p XPS spectrum (Fig. 3c), the peaks at 781.3 eV and 796.5 eV are attributed to Co $2p_{3/2}$ and Co $2p_{1/2}$, respectively, indicating the presence of Co^{3+} and Co^{2+} in the PC/$NiCo_2S_4$ composites. In the high-resolution S 2p spectrum (Fig. 3d), the two peaks at binding energies of 161.6 and 162.7 eV are assigned to S $2p_{3/2}$ and S $2p_{1/2}$, respectively. According to XPS results, the superficial ions in PCs/$NiCo_2S_4$ are Ni^{3+}, Ni^{2+}, Co^{3+}, Co^{2+}, and S^{2-}, which agrees well with other reported works [36,37].

3.3. XRD and Raman analysis

X-ray diffraction (XRD) patterns of the PCs and PCs/$NiCo_2S_4$ composite are shown in Fig. 4(a). The PCs show two characteristic peaks at $2\theta = 24.6^\circ$ and 43.5°, which correspond to (0 0 2) and (1 0 0) reflections, and which indicate the characteristics of amorphous carbon [10]. In the pattern of Ni/Co precursors, the peaks can be well assigned with the $Co(CO_3)_{0.5}(OH)_{0.11}{\cdot}H_2O$ (JCPDS Card No. 48-0083) and $Ni_2(OH)_2CO_3{\cdot}4H_2O$ (JCPDS Card No. 38-0714) [38]. For the PCs/$NiCo_2S_4$ composites, characteristic diffraction peaks of amorphous carbon still exist, simultaneously. A series of new peaks occurs at 31.7°, 38.4° and 55.4°, which correspond to the (3 1 1), (4 0 0), and (4 4 0) reflections of crystalline $NiCo_2S_4$ (JCPDS Card No. 20-0782) [39], and which indicate that the $NiCo_2S_4$ nanoparticles have grown on the PCs. The PC/$NiCo_2S_4$ sample was examined by Raman spectroscopy to obtain detailed information on the structure and the result is shown Fig. 4(b). The presence of a D-band at 1358 cm^{-1} and Ag-band at 1580 cm^{-1} is associated with disordered graphite and ordered graphite, respectively [40]. The D-band and G-band are also related to the *k*-point phonon mode of A_{1g} symmetry and the E_{2g} vibrational mode of the sp^2-bonded carbon atoms. The relatively weak peaks at 517 and 657 cm^{-1} are ascribed to the F_{2g} and A_{1g} stretching modes of $NiCo_2S_4$, respectively [41]. Thus, Raman analysis provides additional information that the $NiCo_2S_4$ has grown on the PCs surface.

3.4. Pore structure analysis

The specific surface area of the PCs and PCs/$NiCo_2S_4$ composites is measured via nitrogen adsorption-desorption isotherms (Fig. 5). The PCs exhibited a combined type-IV adsorption-desorption isotherm with a distinct H3 hysteresis loop at the relative pressure P/P_0 of 0.4–1.0, which indicates that the PCs are microporous and mesoporous materials. A large specific surface area of 1218.4 $m^2\,g^{-1}$ was acquired. Hence, the PCs with a large specific surface area can serve as a substrate to combine with electroactive materials of $NiCo_2S_4$. With the formation of $NiCo_2S_4$ nanoparticles that anchor on the PC surface, $NiCo_2S_4$ will block part of the PC nanopores. As a result, the specific surface area of the PC/$NiCo_2S_4$ composite will decrease and the pore size distribution will also change. However, the specific surface area of the PCs/$NiCo_2S_4$ can still reach 525 $m^2\,g^{-1}$. The PCs/$NiCo_2S_4$ composite with such a specific surface area can provide sufficient contact between electroactive materials and electrolyte solution for the diffusion and migration of electrolyte ions and electrons.

3.5. Electrochemical performance of PCs and PCs/$NiCo_2S_4$ composites

The electrochemical performance of the PCs was investigated by employing a three-electrodes system in 6 M KOH electrolyte. Before testing the CV curves, the electrodes were stabilized by 20 repeated cycles at a scanning rate of 20 mV s^{-1}. As observed in Fig. 6a, the curves of the PCs electrode are nearly rectangular at different scanning rates, even at a high-potential scanning speed of 100 mV s^{-1}, indicating the double-layer capacitance characteristic and excellent rate performance. Fig. 6b shows the GCD curves of PCs under various current densities from 0.5 to 10 A g^{-1}, which exhibited almost linear and triangle shapes, and demonstrates again the excellent ideal capacitance

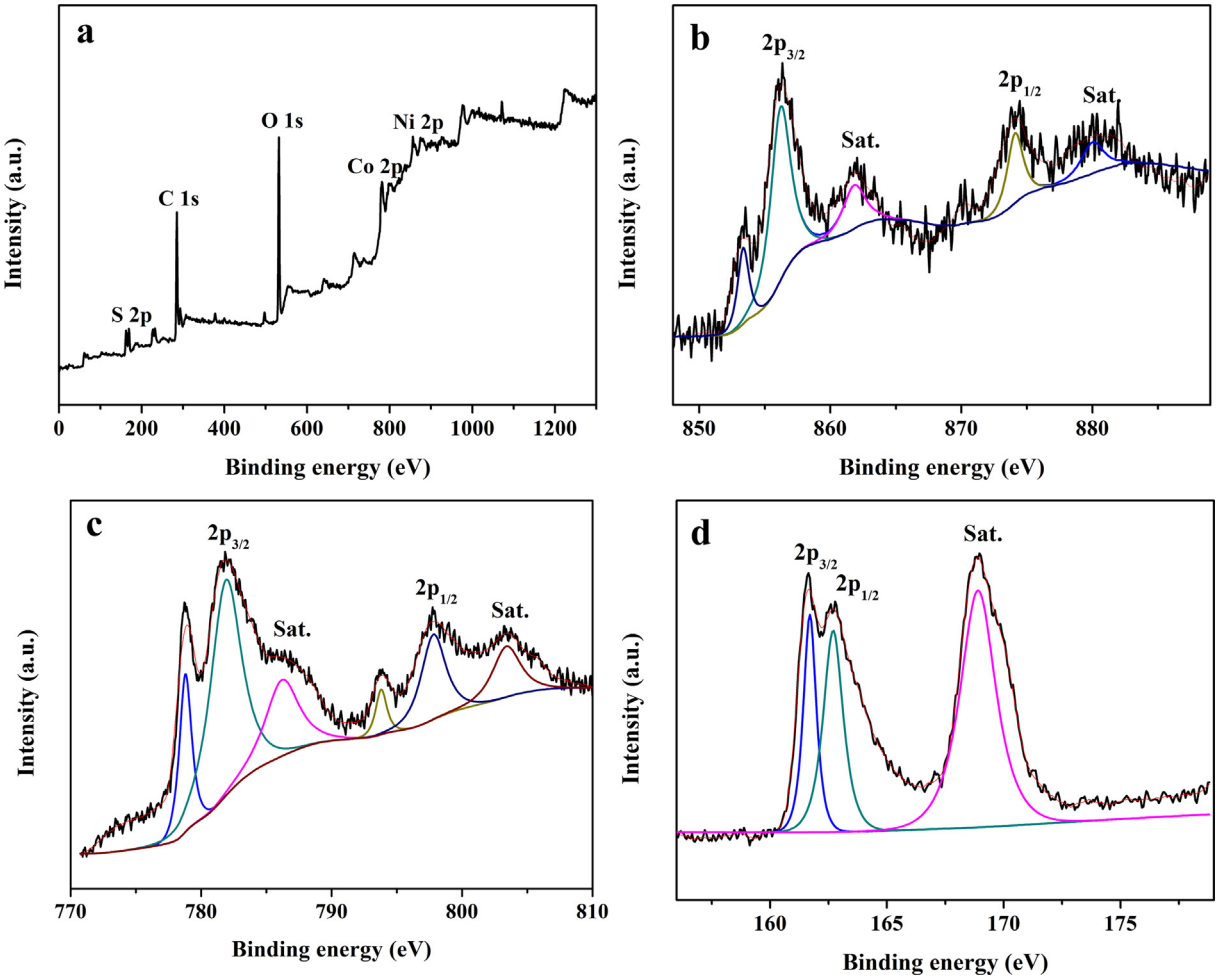

Fig. 3. (a) Full survey scan XPS spectrum of PCs/$NiCo_2S_4$ composites; high-resolution XPS spectrum in the (b) Ni 2p, (c) Co 2p and (d) S 2p regions of the PCs/$NiCo_2S_4$ composites.

behavior and electrochemical invertibility. The specific capacitances of the PCs according to the current densities are calculated separately from the discharge curves and are shown in Fig. 6c. A specific capacitance of 165.8 F g^{-1} could be provided by the PCs electrode at a current density of 0.5 A g^{-1}. The excellent capacitive property of the PCs may be attributed to the highly porous structure and large specific surface area of the materials, which increases the active sites for rapid ion diffusion and charge migration, and shortens the charge diffusion pathway. Fig. 6d indicates that the PCs showed a high capacitance conservation of 96.4% after 5000 charge/discharge cycles, which suggests an outstanding ion migration and electron-transfer process in the long-term cycling.

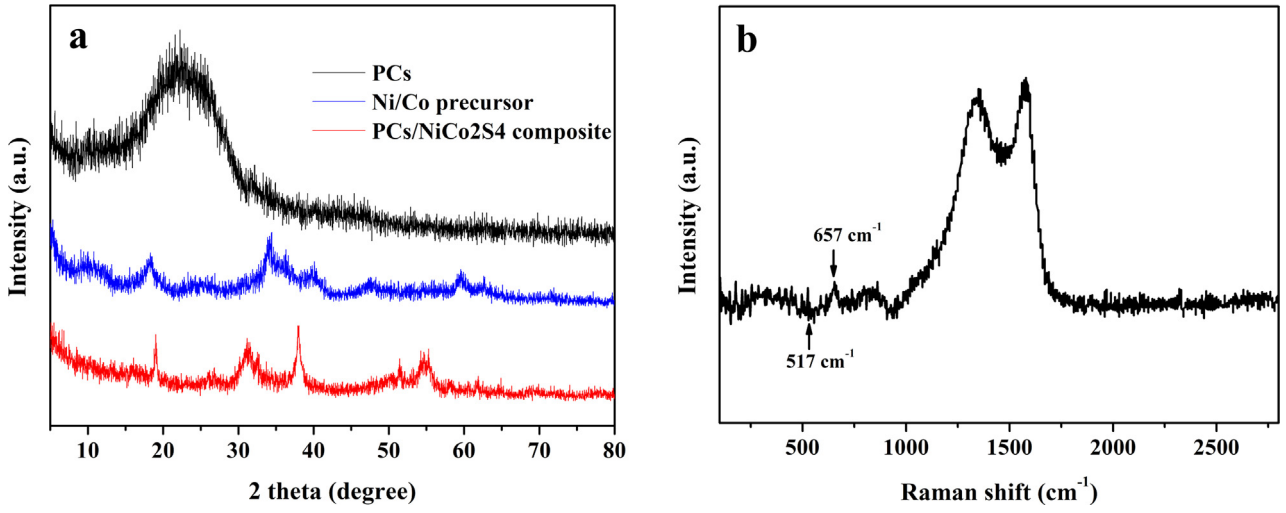

Fig. 4. (a) XRD patterns of PCs, Ni/Co precursors and PCs/$NiCo_2S_4$ composites, (b) Raman spectrum of PCs/$NiCo_2S_4$ composites.

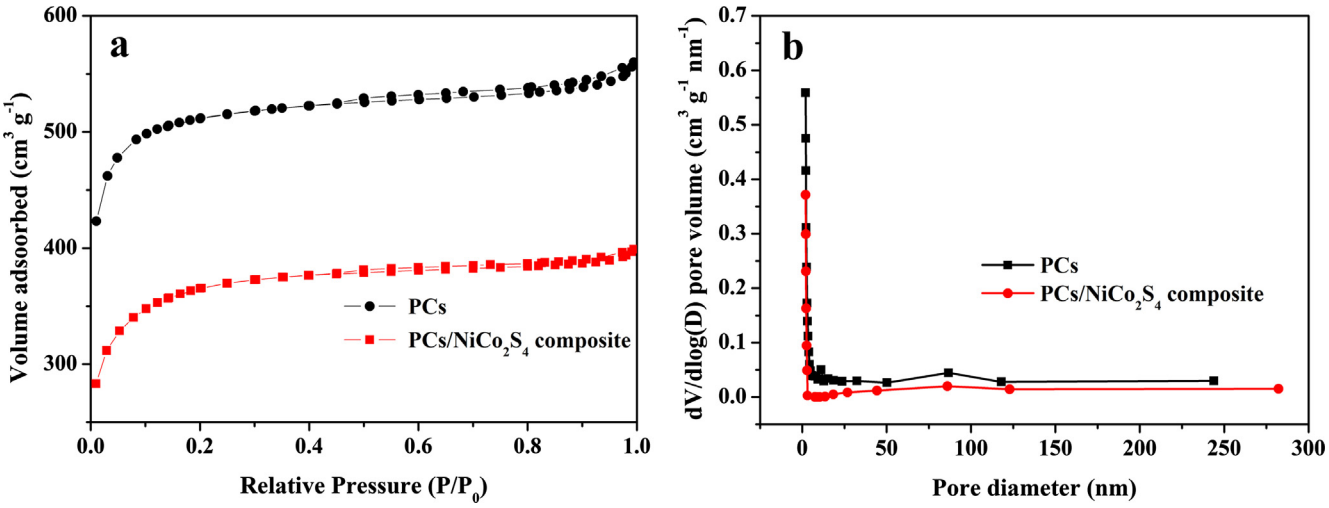

Fig. 5. (a) N_2 adsorption and desorption isotherms and (b) pore size distributions of PCs and PCs/$NiCo_2S_4$ composites.

A PCs/$NiCo_2S_4$ composite was acquired by the hydrothermal growth of $NiCo_2S_4$ using PCs as the electroconductive substrate. All CV curves show a pair of distinct redox peaks under the anodic and cathodic scans, indicating the presence of Faradaic redox reactions. When the scanning rates increased, the anodic peaks moved to higher potential regions while the reduction peaks moved to lower potential regions, demonstrating the presence of rapid redox reactions among the active material and the KOH electrolyte. This phenomenon results because pores in the electrode materials could affect the ion migration and diffusion significantly. At low scanning rates, external and internal pore surfaces of the electrode material can be used effectively for OH^- migration, while under higher scanning speeds, OH^- ion migration is

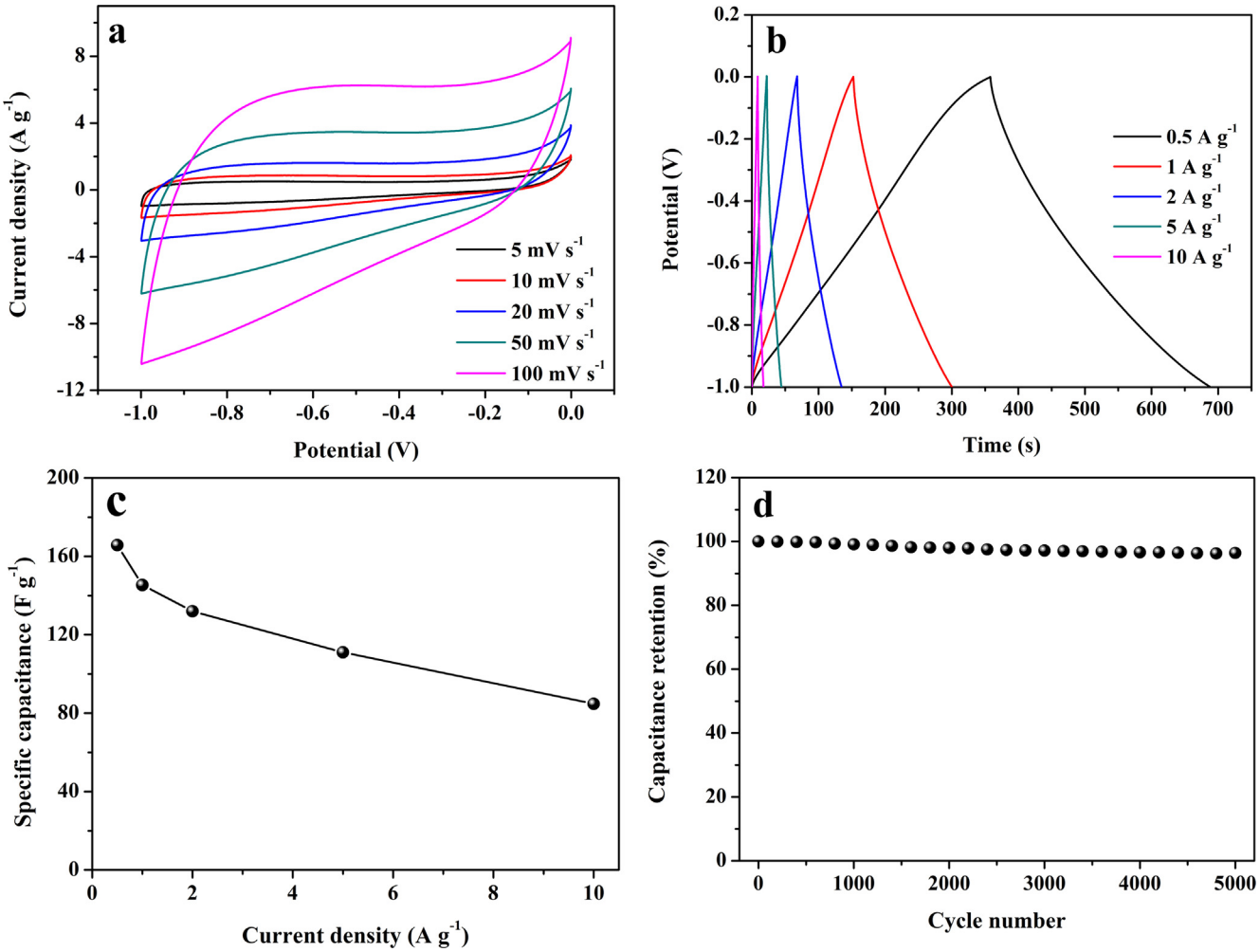

Fig. 6. (a) CV curves of PCs electrode at various scan rates, (b) galvanostatic charge/discharge curves of the PCs electrode at various current densities, (c) calculated specific capacitances of the PCs electrode at various current densities, (d) cycling performance of the PCs electrode at a current density of 10 A g^{-1}.

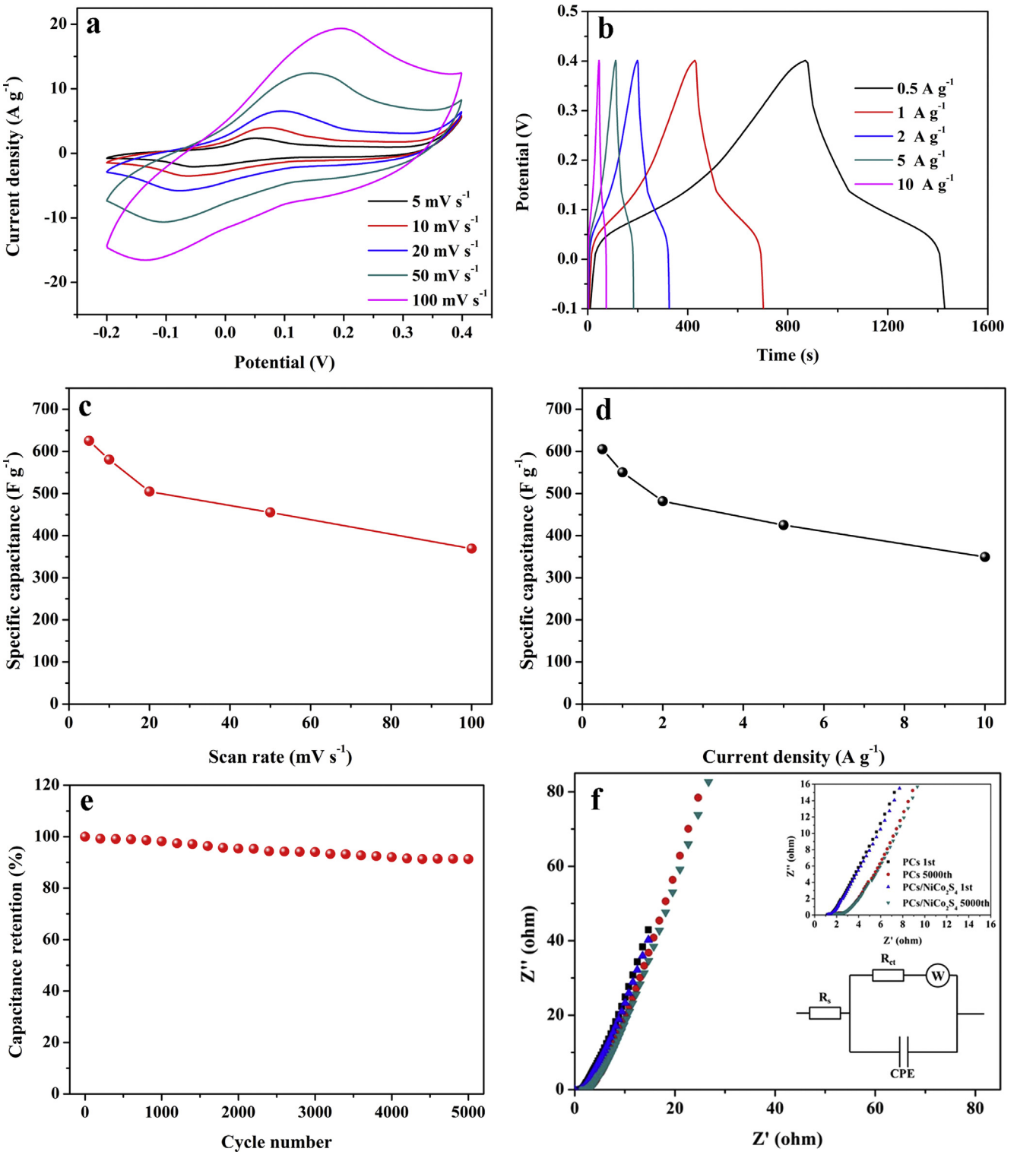

Fig. 7. (a) CV curves of PCs/$NiCo_2S_4$ composites at various scan rates, (b) galvanostatic charge/discharge curves at various current densities for PCs/$NiCo_2S_4$ composites, (c) calculated specific capacitances of the PCs/$NiCo_2S_4$ composites at various scan rates, (d) calculated specific capacitances of the PCs/$NiCo_2S_4$ composites at various current densities, (e) cycling performance of the PCs/$NiCo_2S_4$ composites at a current density of 10 A g^{-1}, (f) Nyquist plots of PCs and PCs/$NiCo_2S_4$ composite electrodes before and after 5000 cycles.

limited by the external area of the pores in the electroactive materials [42]. The CV curves of PCs and PCs/$NiCo_2S_4$ composite are compared in Fig. 7(a). The PCs/$NiCo_2S_4$ composite presents a larger integrated area for the curves than PCs at the scanning rate of 20 mV s^{-1}, which reflects a better pseudocapacitance characteristic of the PCs/$NiCo_2S_4$ composite than pure PCs. The Faradaic reactions that occurred between the electrode material and the alkaline electrolyte are Co^{2+}/Co^{3+}, Co^{3+}/Co^{4+}, and Ni^{2+}/Ni^{3+} on the basis of [31]:

$$CoS + OH^- \leftrightarrow CoSOH + e^-$$

$$CoSOH + OH^- \leftrightarrow CoSO + H_2O + e^-$$

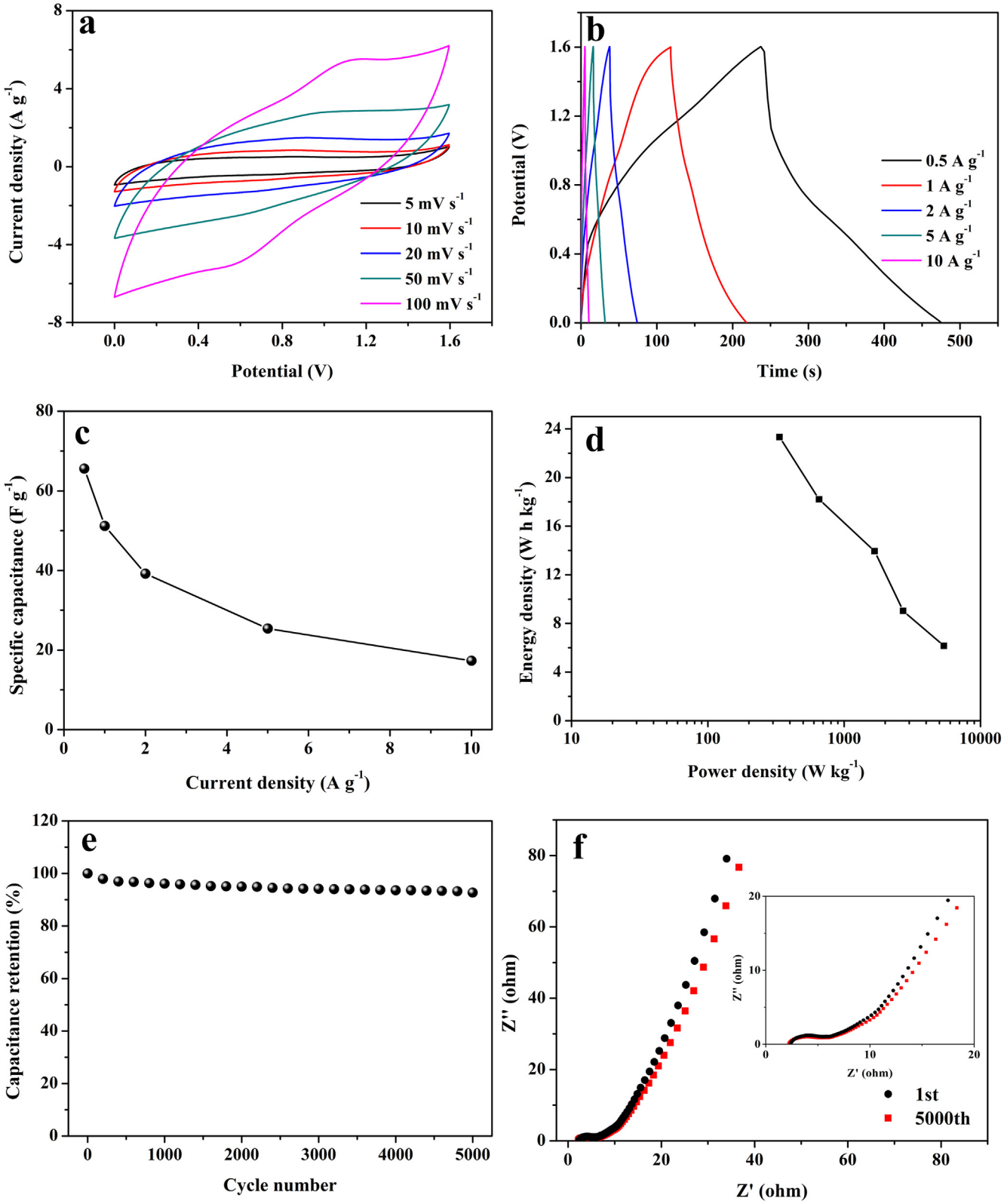

Fig. 8. (a) CV curves of the PCs/$NiCo_2S_4$//PCs asymmetric supercapacitor electrode at various scan rates and (b) galvanostatic charge/discharge curves at various current densities, (c) calculated specific capacitances of the asymmetric supercapacitor electrode at various current densities, (d) Ragone plots of the as-fabricated asymmetric supercapacitor, (e) cycling performance of the asymmetric supercapacitor at the current density of 10 A g^{-1}, (f) Nyquist plots of the asymmetric supercapacitor before and after 5000 cycles.

$$NiS + OH^- \leftrightarrow NiSOH + e^-$$

To investigate the electrochemical capacitive property of the electrodes, galvanostatic charge/discharge (GCD) tests were performed from −0.1 V to 0.4 V at various current densities as presented in Fig. 7(b). All curves have A good symmetry, which suggests the high

coulombic efficiency and superior reversible redox capacities of the electrode materials. The discharge curves of the electrodes drifted from a linear type, which proves the existence of Faradaic redox reactions. All discharge curves show a potential platform, which indicates that the electrode exhibited a typical pseudocapacitance behavior that resulted from charge-migration and electrochemical absorption/desorption processes at the electrode/electrolyte interface. The result agrees with the CV tests analyzed above. The calculated specific capacitances of the PCs/$NiCo_2S_4$ electrode are 625.2 and 369.3 F g^{-1} at the scan rate of 5 and 100 mV s^{-1}, respectively, presented in Fig. 7(c). In addition, as shown in Fig. 7(d), the calculated specific capacitances of the PCs/$NiCo_2S_4$ electrode at current densities from the discharge curves are calculated to be 605.2, 550.6, 481.8, 425.2 and 349.3 F g^{-1}, respectively. The decrease of specific capacitance with increasing current density is due to ion transfer within the highly porous structure lags behind the potential change and the internal resistances for charge carriers retard the capacitive performance of the electrode at higher current density. The long-term stability for PCs/$NiCo_2S_4$ electrode was also investigated, and the result is presented in Fig. 7(e). After 5000 consecutive charge/discharge cycles at the current density of 10 A g^{-1}, the PCs/$NiCo_2S_4$ electrode still possesses a capacitance retention of 91.3%, because of the excellent stability of the PCs substrate, which can meet the commercial demands of pseudocapacitor devices. The excellent electrochemical performances of PCs/$NiCo_2S_4$ electrode may be attributed to: (a) KOH-activation-generated micropores on the outer carbon layer can offer sufficient and highly efficient channels for ion diffusion into the inner carbon layer; (b) the large specific surface area can provide plentiful adsorption sites for electrolyte ions and exhibits a high capability for charge accumulation at the electrode/electrolyte interface, and thus enhances the double-layer capacitances [3]; and (c) the porous structure of the PCs after KOH treatment could offer sufficient superficial active sites for the growth of $NiCo_2S_4$, thus improve the electrochemical property of PCs from reversible Faradaic reactions. The electrochemical properties of the electrode material are related mainly to ion diffusion and charge migration. A comparison of the electrical conductivity of pure PCs electrode and PCs/$NiCo_2S_4$ composite electrode can be obtained from the EIS results as shown in Fig. 7(f). The simulative equivalent circuit model is shown in the insert, where R_s represents the solution resistance arising from the electrolyte, R_{ct} represents the charge transfer resistance, CPE represents the constant phase element related to the interfacial resistance and Z_w is the Warburg impedance. All curves are consisted of a nearly semicircle at high-frequency and a nearly straight line exists in the low-frequency. The real axis intercede at high-frequency region represents the R_s for the electrode, consisting mainly of an intrinsic impedance of the electrodes, the electrolyte impedance and the contact impedance between the electrodes and the electrolyte. The semicircle diameter of the Nyquist image represents R_{ct}, arising from the uncontinuity during the charge-migration process on the surface [40]. As shown in the inset of Fig. 8, the PCs/$NiCo_2S_4$ electrode exhibits a larger depressed semicircle than the PCs electrode at high-frequency, which suggests a higher charge-migration resistance at the electrode interface because of the existence of $NiCo_2S_4$. Nevertheless, the electrode could still provide a sufficient pathway for ionic diffusion and electron migration. In addition, the Nyquist plots of the electrodes were also measured after 5000 cycles. It can be seen that, the R_s and R_{ct} remained almost unchanged, further indicating the stability of the electrode samples.

3.6. Electrochemical performance of the asymmetric supercapacitor

To investigate the electrochemical performance of PCs/$NiCo_2S_4$ composites for potential energy storage application, an asymmetric supercapacitor was fabricated by using PCs/$NiCo_2S_4$ composites as the positive electrode and PCs as the negative electrode, respectively. Fig. 8(a) shows the corresponding CV curves of the asymmetric supercapacitor at various scanning rates. It can be seen that, the CV curves of the asymmetric supercapacitor exhibits no obvious distortion even at a high scanning rate of 100 mV s^{-1}. GCD curves and the corresponding specific capacitances of the fabricated asymmetric supercapacitor at various current densities are shown in Fig. 8(b) and (c), the specific capacitances are calculated to be 65.6, 51.2, 39.2, 25.4 and 17.3 F g^{-1} at current densities of 0.5, 1, 2, 5 and 10 A g^{-1}, respectively. Moreover, the corresponding Ragone plots of the supercapacitor are measured from the discharge curves as shown in Fig. 8(d). The asymmetric supercapacitor shows a high energy density of 23.3 W h kg^{-1} at the power density of 335.8 W kg^{-1}. Meanwhile, the asymmetric supercapacitor device also presents an excellent electrochemical stability with ~92.7% capacitance retention at the current density of 10 A g^{-1} after 5000 consecutive charge/discharge cycles (Fig. 8e), indicating its potential application in the field of energy storage. In addition, the Nyquist plots of the asymmetric supercapacitor before and after 5000 charge/discharge cycles were also measured as shown in Fig. 8(f). The R_s and R_{ct} values remained unchanged before and after 5000cycling except a slight change in the Warburg impedance (Z_w) due to the shear active surface areas of active materials during long cycling.

4. Conclusions

In summary, PCs and PCs/$NiCo_2S_4$ composites have been prepared by using popcorn as a carbon source and substrate. Ball-like $NiCo_2S_4$ nanoparticles were obtained by a hydrothermal process and a specific surface area of 525 m^2 g^{-1} was acquired for the PCs/$NiCo_2S_4$ composites. Due to the hydrothermal growth of $NiCo_2S_4$, and with the combination between the $NiCo_2S_4$ nanoparticles and the highly conductive PCs substrate, the PCs/$NiCo_2S_4$ composite can provide adequate active sites to enable rapid electron transfer and electrolyte ion diffusion. As a result, the PCs/$NiCo_2S_4$ composite electrode delivers a specific capacitance of 605.2 F g^{-1} at 0.5 A g^{-1} and exhibits a capacitance conservation of 91.3% at 10 A g^{-1} with a prominent electrochemical stability of 91.3% capacitance retention. The fabricated asymmetric supercapacitor can deliver a high energy density 23.3 W h kg^{-1} at the power density of 335.8 W kg^{-1}. Hence, the obtained PCs/$NiCo_2S_4$ composite can be used as a potential electrode material on supercapacitors in energy-storage applications.

Acknowledgments

The Fundamental Research Funds for Central Universities (E2572017EB05) and Heilongjiang Province outstanding youth science fund (JC201301) is acknowledged.

References

[1] Y. Yang, F. Yang, H. Hu, S. Lee, Y. Wang, H. Zhao, D. Zeng, B. Zhou, S. Hao, Dilute NiO/carbon nanofiber composites derived from metal organic framework fibers as electrode materials for supercapacitors, Chem. Eng. J. 307 (2017) 583–592.
[2] X. Xia, D. Chao, Z. Fan, C. Guan, X. Cao, H. Zhang, H.J. Fan, A new type of porous graphite foams and their integrated composites with oxide/polymer core/shell nanowires for supercapacitors: structural design, fabrication, and full supercapacitor demonstrations, Nano Letters 14 (2014) 1651–1658.
[3] M. Liu, X. Wang, D. Zhu, L. Li, H. Duan, Z. Xu, Z. Wang, L. Gan, Encapsulation of NiO nanoparticles in mesoporous carbon nanospheres for advanced energy storage, Chem. Eng. J. 308 (2017) 240–247.
[4] I. Oh, M. Kim, J. Kim, Carbon-coated Si/MnO_2 nanoneedle composites with optimum carbon layer activation for supercapacitor applications, Chem. Eng. J. 273 (2015) 82–91.
[5] W. Lu, M. Liu, L. Miao, D. Zhu, X. Wang, H. Duan, Z. Wang, L. Li, Z. Xu, L. Gan, L. Chen, Nitrogen-containing ultramicroporous carbon nanospheres for high performance supercapacitor electrodes, Electrochimica Acta 205 (2016) 132–141.
[6] Z. Tang, C.-H. Tang, H. Gong, A high energy density asymmetric supercapacitor from nano-architectured $Ni(OH)_2$/carbon nanotube electrodes, Adv. Funct. Mater. 22 (2012) 1272–1278.
[7] V. Ruiz, C. Blanco, R. Santamaría, J.M. Ramos-Fernández, M. Martínez-Escandell, A. Sepúlveda-Escribano, F. Rodríguez-Reinoso, An activated carbon monolith as an electrode material for supercapacitors, Carbon 47 (2009) 195–200.
[8] G. Zu, J. Shen, L. Zou, F. Wang, X. Wang, Y. Zhang, X. Yao, Nanocellulose-derived highly porous carbon aerogels for supercapacitors, Carbon 99 (2016) 203–211.

[9] M. Yan, Y. Yao, J. Wen, L. Long, M. Kong, G. Zhang, X. Liao, G. Yin, Z. Huang, Construction of a hierarchical $NiCo_2S_4$@PPy core-shell heterostructure nanotube array on Ni foam for a high-performance asymmetric supercapacitor, ACS Appl. Mater. Interfaces 8 (2016) 24525–24535.

[10] I.I.G. Inal, S.M. Holmes, A. Banford, Z. Aktas, The performance of supercapacitor electrodes developed from chemically activated carbon produced from waste tea, Appl. Surf. Sci. 357 (2015) 696–703.

[11] V. Sahu, S. Grover, B. Tulachan, M. Sharma, G. Srivastava, M. Roy, M. Saxena, N. Sethy, K. Bhargava, D. Philip, H. Kim, G. Singh, S.K. Singh, M. Das, R.K. Sharma, Heavily nitrogen doped, graphene supercapacitor from silk cocoon, Electrochim. Acta 160 (2015) 244–253.

[12] Z.Y. Sui, Y.N. Meng, P.W. Xiao, Z.Q. Zhao, Z.X. Wei, B.H. Han, Nitrogen-doped graphene aerogels as efficient supercapacitor electrodes and gas adsorbents, ACS Appl. Mater. Interfaces 7 (2015) 1431–1438.

[13] P. Geng, S. Zheng, H. Tang, R. Zhu, L. Zhang, S. Cao, H. Xue, H. Pang, Transition metal sulfides based on graphene for electrochemical energy storage, Adv. Energy Mater. 8 (2018) 1703259.

[14] L. Jiang, L. Sheng, C. Long, Z. Fan, Densely packed graphene nanomesh-carbon nanotube hybrid film for ultra-high volumetric performance supercapacitors, Nano Energy 11 (2015) 471–480.

[15] D. Yu, S. Zhai, W. Jiang, K. Goh, L. Wei, X. Chen, R. Jiang, Y. Chen, Transforming pristine carbon fiber tows into high performance solid-state fiber supercapacitors, Adv. Mater. 27 (2015) 4895–4901.

[16] P. Suktha, P. Chiochan, P. Iamprasertkun, J. Wutthiprom, N. Phattharasupakun, M. Suksomboon, T. Kaewsongpol, P. Sirisinudomkit, T. Pettong, M. Sawangphruk, High-performance supercapacitor of functionalized carbon fiber paper with high surface ionic and bulk electronic conductivity: effect of organic functional groups, Electrochim. Acta 176 (2015) 504–513.

[17] H. Zhuo, Y. Hu, X. Tong, L. Zhong, X. Peng, R. Sun, Sustainable hierarchical porous carbon aerogel from cellulose for high-performance supercapacitor and CO_2 capture, Ind. Crops Prod. 87 (2016) 229–235.

[18] M. Oschatz, S. Boukhalfa, W. Nickel, J.P. Hofmann, C. Fischer, G. Yushin, S. Kaskel, Carbide-derived carbon aerogels with tunable pore structure as versatile electrode material in high power supercapacitors, Carbon 113 (2017) 283–291.

[19] Z.-Y. Li, M.S. Akhtar, O.B. Yang, Supercapacitors with ultrahigh energy density based on mesoporous carbon nanofibers: enhanced double-layer electrochemical properties, J. Alloy. Compd. 653 (2015) 212–218.

[20] C. Liu, J. Wang, J. Li, M. Zeng, R. Luo, J. Shen, X. Sun, W. Han, L. Wang, Synthesis of N-doped hollow-structured mesoporous carbon nanospheres for high-performance supercapacitors, ACS Appl. Mater. Interfaces 8 (2016) 7194–7204.

[21] Q. Li, Y. Xu, S. Zheng, X. Guo, H. Xue, H. Pang, Recent progress in some amorphous materials for supercapacitors, Small 14 (2018) 1800426.

[22] J. Jiang, Y. Li, J. Liu, X. Huang, C. Yuan, X.W. Lou, Recent advances in metal oxide-based electrode architecture design for electrochemical energy storage, Adv. Mater. 24 (2012) 5166–5180.

[23] H. Wan, X. Ji, J. Jiang, J. Yu, L. Miao, L. Zhang, S. Bie, H. Chen, Y. Ruan, Hydrothermal synthesis of cobalt sulfide nanotubes: the size control and its application in supercapacitors, J. Power Sources 243 (2013) 396–402.

[24] H. Li, Y. Gao, Y. Shao, Y. Su, X. Wang, Vapor-phase atomic layer deposition of Co_9S_8 and its application for supercapacitors, Nano Letters 15 (2015) 6689–6695.

[25] R. Xu, J. Lin, J. Wu, M. Huang, L. Fan, X. He, Y. Wang, Z. Xu, Hydrothermal synthesis of $CoMoO_4/Co_9S_8$ nanorod arrays on nickel foam for high-performance asymmetric supercapacitors with high energy density, Electrochim. Acta 252 (2017) 470–481.

[26] X. Li, Q. Li, Y. Wu, M. Rui, H. Zeng, Two-dimensional, porous nickel-cobalt sulfide for high-performance asymmetric supercapacitors, ACS Appl. Mater. Interfaces 7 (2015) 19316–19323.

[27] M. Liang, M. Zhao, H. Wang, J. Shen, X. Song, Enhanced cycling stability of hierarchical $NiCo_2S_4$@$Ni(OH)_2$@PPy core–shell nanotube arrays for aqueous asymmetric supercapacitors, J. Mater. Chem. A 6 (2018) 2482–2493.

[28] F. Yu, Z. Chang, X. Yuan, F. Wang, Y. Zhu, L. Fu, Y. Chen, H. Wang, Y. Wu, W. Li, Ultrathin $NiCo_2S_4$@graphene with a core–shell structure as a high performance positive electrode for hybrid supercapacitors, J. Mater. Chem. A 6 (2018) 5856–5861.

[29] J. Pu, F. Cui, S. Chu, T. Wang, E. Sheng, Z. Wang, Preparation and electrochemical characterization of hollow hexagonal $NiCo_2S_4$ nanoplates as pseudocapacitor materials, ACS Sustain. Chem. Eng 2 (2014) 809–815.

[30] H. Wan, J. Jiang, J. Yu, K. Xu, L. Miao, L. Zhang, H. Chen, Y. Ruan, $NiCo_2S_4$ porous nanotubes synthesis via sacrificial templates: high-performance electrode materials of supercapacitors, Cryst. Eng. Comm 15 (2013) 7649–7651.

[31] J. Xiao, L. Wan, S. Yang, F. Xiao, S. Wang, Design hierarchical electrodes with highly conductive $NiCo_2S_4$ nanotube arrays grown on carbon fiber paper for high-performance pseudocapacitors, Nano Letters 14 (2014) 831–838.

[32] J. Hou, K. Jiang, R. Wei, M. Tahir, X. Wu, M. Shen, X. Wang, C. Cao, Popcorn-derived porous carbon flakes with an ultrahigh specific surface area for superior performance supercapacitors, ACS Appl. Mater. Interfaces 9 (2017) 30626–30634.

[33] T. Liang, C. Chen, X. Li, J. Zhang, Popcorn-derived porous carbon for energy storage and CO_2 capture, Langmuir ACS J. Surf. Colloids 32 (2016) 8042–8049.

[34] D.P. Dubal, N.R. Chodankar, Z. Caban-Huertas, F. Wolfart, M. Vidotti, R. Holze, C.D. Lokhande, P. Gomez-Romero, Synthetic approach from polypyrrole nanotubes to nitrogen doped pyrolyzed carbon nanotubes for asymmetric supercapacitors, J. Power Sources 308 (2016) 158–165.

[35] X. Ning, F. Li, Y. Zhou, Y.-E. Miao, C. Wei, T. Liu, Confined growth of uniformly dispersed $NiCo_2S_4$ nanoparticles on nitrogen-doped carbon nanofibers for high-performance asymmetric supercapacitors, Chem. Eng. J. 328 (2017) 599–608.

[36] J. Pu, F. Cui, S. Chu, T. Wang, E. Sheng, Z. Wang, Preparation and electrochemical characterization of hollow hexagonal $NiCo_2S_4$ nanoplates as pseudocapacitor materials, ACS Sustain. Chem. Eng. 2 (2013) 809–815.

[37] J. Chen, J. Xu, S. Zhou, N. Zhao, C.-P. Wong, Nitrogen-doped hierarchically porous carbon foam: A free-standing electrode and mechanical support for high-performance supercapacitors, Nano Energy 25 (2016) 193–202.

[38] Y. Zheng, J. Xu, X. Yang, Y. Zhang, Y. Shang, X. Hu, Decoration $NiCo_2S_4$ nanoflakes onto Ppy nanotubes as core-shell heterostructure material for high-performance asymmetric supercapacitor, Chem. Eng. J. 333 (2018) 111–121.

[39] X. Liang, K. Nie, X. Ding, L. Dang, J. Sun, F. Shi, H. Xu, R. Jiang, X. He, Z. Liu, Z. Lei, Highly compressible carbon sponge supercapacitor electrode with enhanced performance by growing nickel-cobalt sulfide nanosheets, ACS Appl. Mater. Interfaces 10 (2018) 10087–10095.

[40] G. Wang, C. Pan, L. Wang, Q. Dong, C. Yu, Z. Zhao, J. Qiu, Activated carbon nanofiber webs made by electrospinning for capacitive deionization, Electrochim. Acta 69 (2012) 65–70.

[41] Y. Gao, Q. Lin, G. Zhong, Y. Fu, X. Ma, Novel $NiCo_2S_4$/graphene composites synthesized via a one-step in-situ hydrothermal route for energy storage, J. Alloy. Compd. 704 (2017) 70–78.

[42] M.K. Sahoo, G.R. Rao, Fabrication of $NiCo_2S_4$ nanoball embedded nitrogen doped mesoporous carbon on nickel foam as an advanced charge storage material, Electrochim. Acta 268 (2018) 139–149.